

Efficient Large Scale Electromagnetics Simulations Using Dynamically Adapted Meshes with the Discontinuous Galerkin Method

Sascha M. Schnell¹

*Graduate School of Computational Engineering, Technische Universitaet Darmstadt,
Dolivostrasse 15, 64293 Darmstadt, Germany*

Thomas Weiland

*Institut fuer Theorie Elektromagnetischer Felder, Technische Universitaet Darmstadt,
Schlossgartenstrasse 8, 64289 Darmstadt, Germany*

Abstract

A framework for performing dynamic mesh adaptation with the discontinuous Galerkin method (DGM) is presented. Adaptations include modifications of the local mesh step size (h -adaptation) and the local degree of the approximating polynomials (p -adaptation) as well as their combination. The computation of the approximation within locally adapted elements is based on projections between finite element spaces (FES), which are shown to preserve the upper limit of the electromagnetic energy. The formulation supports high level hanging nodes and applies precomputation of surface integrals for increasing computational efficiency. A full wave simulation of electromagnetic scattering from a radar reflector demonstrates the applicability to large scale problems in three-dimensional space.

Keywords: Discontinuous Galerkin method, dynamic mesh adaptation,

hp-adaptation, Maxwell time-domain problem, large scale simulations

2000 MSC: 65M60, 78A25

Email addresses: schnell@gsc.tu-darmstadt.de (Sascha M. Schnell),
weiland@temf.tu-darmstadt.de (Thomas Weiland)

¹The work of S. Schnell is supported by the 'Initiative for Excellence' of the German Federal and State Governments and the Graduate School of Computational Engineering at Technische Universitaet Darmstadt.

1. Introduction

The discontinuous Galerkin method [1, 2] nowadays is a well-established method for solving partial differential equations, especially for time-dependent problems. It has been thoroughly investigated by Cockburn and Shu as well as Hesthaven and Warburton, who summarized many of their findings in [3] and [4], respectively. Concerning Maxwell's equations in time-domain, the DGM has been studied in particular in [5, 6, 7, 8]. The former two apply tetrahedral meshes, which provide flexibility for the generation of meshes also for complicated structures. The latter two make use of hexahedral meshes, which allow for a computationally more efficient implementation [9].

In [3] the authors state that the method can easily deal with meshes with hanging nodes since no inter-element continuity is required, which renders it particularly well suited for hp -adaptivity. Indeed, many works are concerned with h -, p - or hp -adaptivity within the DG framework. The first published work of this kind is presumably [10], where the authors consider linear scalar hyperbolic conservation laws in two space dimensions. For a selection of other publications see [11, 12, 13, 14, 15] and references therein. The latter three are concerned with the adaptive solution of Maxwell's equations in the time-harmonic case.

In this article, we are concerned with solving the Maxwell equations for electromagnetic fields with arbitrary time dependence in a three-dimensional domain $\Omega \subset \mathbb{R}^3$. They read

$$\nabla \times \mathbf{E}(\mathbf{r}, t) = -\frac{\partial}{\partial t} \mathbf{B}(\mathbf{r}, t), \quad (1a)$$

$$\nabla \times \mathbf{H}(\mathbf{r}, t) = \frac{\partial}{\partial t} \mathbf{D}(\mathbf{r}, t) + \mathbf{J}(\mathbf{r}, t), \quad (1b)$$

with the spatial variable $\mathbf{r} \in \Omega$ and the temporal variable t subject to boundary conditions specified at the domain boundary $\partial\Omega$ and initial conditions specified at time t_0 . The vectors of the electric field and flux density are denoted by \mathbf{E} and \mathbf{D} and the vectors of the magnetic field and flux density by \mathbf{H} and \mathbf{B} . The electric current density is denoted by \mathbf{J} . However, we assume the domain to be source free and free of conductive currents ($\mathbf{J} = \mathbf{0}$). Furthermore, we assume heterogeneous, linear, isotropic, non-dispersive and

time-independent materials in the constitutive relations

$$\mathbf{B}(\mathbf{r}, t) = \mu(\mathbf{r}) \mathbf{H}(\mathbf{r}, t), \quad (2a)$$

$$\mathbf{D}(\mathbf{r}, t) = \epsilon(\mathbf{r}) \mathbf{E}(\mathbf{r}, t). \quad (2b)$$

The material parameters μ and ϵ are the magnetic permeability and dielectric permittivity. At the domain boundary, we apply either electric ($\mathbf{n} \times \mathbf{E} = \mathbf{0}$) or radiation boundary conditions ($\mathbf{n} \times \mathbf{E} = c\mu(\mathbf{n} \times \mathbf{n} \times \mathbf{H})$), where c denotes the local speed of light $c = (\epsilon\mu)^{-1/2}$. We also introduce the electromagnetic energy W contained in a volume V obtained by integrating the energy density w as

$$W(t) = \int_V w(t) d^3\mathbf{r} = \int_V \frac{1}{2} (\epsilon(\mathbf{r}) \mathbf{E}(\mathbf{r}, t)^2 + \mu(\mathbf{r}) \mathbf{H}(\mathbf{r}, t)^2) d^3\mathbf{r}. \quad (3)$$

In [16] we presented a strategy for performing hp -adaptations based on a posteriori error estimation in one-dimensional space, which is summarized briefly in Sec. 4. As the extension of this strategy to three-dimensional space is subject of ongoing work, we drive the grid adaptation using physical properties of the solution, i.e., the local energy density.

This paper focuses on a general formulation of the DGM on non-regular hexahedral meshes as well as the projection of solutions during mesh adaptation. The issues of optimality of the projections and stability of the adaptive algorithm are addressed. Special emphasis is put on discussing the computational efficiency. To the best of our knowledge, this is the first publication dealing with dynamical hp -meshes for the Maxwell time-domain problem employing the DG method in three-dimensional space.

2. Discontinuous Galerkin discretization on non-regular hexahedral grids

2.1. Discretization of space

We perform a tessellation of the domain of interest Ω into N hexahedra \mathcal{T}_i such that the tessellation $\mathcal{T} = \bigcup_{i=1}^N \mathcal{T}_i$ is a polyhedral approximation of Ω . The tessellation is not required to be regular, however, it is assumed to be derivable from a regular root tessellation \mathcal{T}^0 by means of element bisections. The number of element bisections along each Cartesian coordinate is referred to as the refinement levels $L_{x,i}, L_{y,i}, L_{z,i}$. As we allow for anisotropic bisecting the refinement levels of one element may differ. The intersection of two

neighboring elements $\mathcal{T}_i \cap \mathcal{T}_k$ is called their interface, which we denote as \mathcal{I}_{ik} . As we consider non-regular grids, every face \mathcal{F}_j of a hexahedral element may be partitioned into several interfaces depending on the number of neighbors K such that $\mathcal{F}_j = \bigcup_{k=1}^K \mathcal{I}_{ik}$. The face orientation is described by the outward pointing unitary normal \mathbf{n}_j . The union of all faces is denoted as \mathcal{F} , and the internal faces $\mathcal{F} \setminus \partial\Omega$ are denoted as \mathcal{F}^{int} . Finally, the volume, area and length measures of elements, interfaces, faces and edges are referred to as $|\mathcal{T}_i|$, $|\mathcal{I}_{ik}|$, $|\mathcal{F}_j|$ and $|\mathcal{T}_{d,i}|$, where d denotes any of the Cartesian coordinates. Every element of the tesselation \mathcal{T} is related to a master element $\hat{\mathcal{T}} = [-1, 1]^3$ through the mapping G_i

$$G_i : \hat{\mathcal{T}} \rightarrow \mathcal{T}_i : \hat{\mathbf{r}} \mapsto \mathbf{r} = \left(\frac{\hat{x}|\mathcal{T}_{x,i}|}{2} + x_{i,0}, \frac{\hat{y}|\mathcal{T}_{y,i}|}{2} + y_{i,0}, \frac{\hat{z}|\mathcal{T}_{z,i}|}{2} + z_{i,0} \right), \quad (4)$$

where $d_{i,0}$ denotes the element center.

2.2. General formulation

Multiplying Maxwell's equations (1) by a test function $\psi(\mathbf{r}) \in H^1(\mathcal{T}_i)$, integrating over \mathcal{T}_i and performing integration by parts yields

$$\int_{\mathcal{T}_i} \left(\psi \mu \frac{\partial}{\partial t} \mathbf{H} - (\nabla \psi) \times \mathbf{E} \right) d^3 \mathbf{r} + \int_{\partial \mathcal{T}_i} \psi (\mathbf{n} \times \mathbf{E}) d^2 \mathbf{r} = 0, \quad (5a)$$

$$\int_{\mathcal{T}_i} \left(\psi \epsilon \frac{\partial}{\partial t} \mathbf{E} + (\nabla \psi) \times \mathbf{H} \right) d^3 \mathbf{r} - \int_{\partial \mathcal{T}_i} \psi (\mathbf{n} \times \mathbf{H}) d^2 \mathbf{r} = 0, \quad (5b)$$

where the explicit dependencies of \mathbf{r} and t have been omitted. Equations (5) constitute the generic weak formulation of the time-dependent Maxwell's equations. In the following, we will replace the exact field solutions \mathbf{E} and \mathbf{H} by approximations using the discontinuous Galerkin framework.

The space and time continuous electromagnetic field quantities are approximated on \mathcal{T} as

$$\mathbf{U}(\mathbf{r}, t) \approx \mathbf{U}_h(\mathbf{r}, t) = \bigoplus_{i=1}^N \mathbf{U}_i(\mathbf{r}, t), \quad (6)$$

where $\mathbf{U} \in \{\mathbf{E}, \mathbf{H}\}$. The element-local approximation $\mathbf{U}_i(\mathbf{r}, t)$ reads

$$\mathbf{U}_i(\mathbf{r}, t) = \sum_p \mathbf{u}_i^p(t) \varphi_i^p(\mathbf{r}) \quad (7)$$

with the polynomial basis functions $\varphi(\mathbf{r})$ and the time-dependent vector of coefficients

$$\mathbf{u}_i^p(t) = [u_{x,i}^p(t), u_{y,i}^p(t), u_{z,i}^p(t)]^T, \quad (8)$$

representing the numerical degrees of freedom. The basis functions are defined with element-wise compact support, which is an essential property of DG methods

$$\varphi_i^p(\mathbf{r}) = \begin{cases} \varphi^p(\mathbf{r}), & \mathbf{r} \in \mathcal{T}_i, \\ 0, & \text{otherwise.} \end{cases} \quad (9)$$

We define the basis functions on the master element $\hat{\mathcal{T}}$ and obtain the element-specific basis through the mapping G_i as

$$\varphi_i = \hat{\varphi} \circ G_i^{-1} \quad (10)$$

We employ Cartesian grids and tensor product basis functions of the form

$$\hat{\varphi}^p(\hat{\mathbf{r}}) = \bigotimes_{d \in \{x,y,z\}} \hat{\varphi}^{p_d}(\hat{r}_d), \quad (11)$$

where p is a multi-index obtained from all $p_d = 0..P_d$. We denote by $P_i = (P_{x,i}, P_{y,i}, P_{z,i})$ the local maximum approximation orders of element \mathcal{T}_i . The finite element space (FES) \mathcal{V}^P spanned by the basis functions is given by the tensor product of the respective one-dimensional spaces

$$\mathcal{V}^P = \mathcal{V}_x^{P_x} \otimes \mathcal{V}_y^{P_y} \otimes \mathcal{V}_z^{P_z} \quad \text{with} \quad \mathcal{V}_d^{P_d} = \text{span}\{\hat{\varphi}^{p_d}(\hat{r}_d); 0 \leq p_d \leq P_d\} \quad (12)$$

The approximation may, thus, make use of different orders P_d in each of the coordinate directions. The basis functions are Legendre polynomials scaled such that [8]

$$\int_{\mathcal{T}_i} \varphi_i^p(\mathbf{r}) \varphi_i^q(\mathbf{r}) d^3\mathbf{r} = \begin{cases} |\mathcal{T}_i|, & p = q \\ 0, & \text{otherwise.} \end{cases} \quad (13)$$

In the following the dependence of the spatial and temporal variable is not written down explicitly.

If now we were to substitute the exact electromagnetic field solution $\{\mathbf{E}, \mathbf{H}\}$ for its approximation the surface integral term of (5) cannot be evaluated straightforwardly at the internal faces \mathcal{F}^{int} . This is due to the ambiguity of the DG approximation at any interface as a result of (6) and (9). Weak

continuity at internal faces is obtained locally by introducing numerical interface fluxes as

$$\int_{\partial\mathcal{T}_i} \psi (\mathbf{n} \times \mathbf{U}^*) d^2\mathbf{r}, \quad (14)$$

where \mathbf{U}^* is a unique interface value computed solely from \mathbf{U}_i and \mathbf{U}_k , where \mathcal{T}_k is a neighboring element. Common choices include centered and upwind fluxes. The centered interface value is given as

$$U_{d,ik}^* = \frac{1}{2} (U_{d,k|\mathcal{I}_{ik}} + U_{d,i|\mathcal{I}_{ik}}). \quad (15)$$

Computing the upwind value is more involved. It is obtained as the exact solution of Maxwell's equations for piece-wise constant initial data after an infinitesimal time span, which is referred to as the Riemannian problem [17]. For the x -component of the electric and magnetic field at an interface with normal \mathbf{n}_z they read

$$E_{x,ik}^* = \frac{(Y_{k|\mathcal{I}_{ik}} E_{x,k|\mathcal{I}_{ik}} - H_{y,k|\mathcal{I}_{ik}}) + (Y_{i|\mathcal{I}_{ik}} E_{x,i|\mathcal{I}_{ik}} + H_{y,i|\mathcal{I}_{ik}})}{Y_{k|\mathcal{I}_{ik}} + Y_{i|\mathcal{I}_{ik}}}, \quad (16a)$$

$$H_{x,ik}^* = \frac{(Z_{k|\mathcal{I}_{ik}} H_{x,k|\mathcal{I}_{ik}} + E_{y,k|\mathcal{I}_{ik}}) + (Z_{i|\mathcal{I}_{ik}} H_{x,i|\mathcal{I}_{ik}} - E_{y,i|\mathcal{I}_{ik}})}{Z_{k|\mathcal{I}_{ik}} + Z_{i|\mathcal{I}_{ik}}}. \quad (16b)$$

with the intrinsic impedance and admittance

$$Z = \sqrt{\frac{\epsilon}{\mu}}, \quad Y = \frac{1}{Z}. \quad (17)$$

Other components are obtained by cycling the component indices and signs [18].

Note that centered fluxes preserve the Hamiltonian structure of Maxwell's equations while this property does not carry over to the semi-discrete equations when applying upwind fluxes due to the mixing of electric and magnetic quantities in (16). Consequently, an energy conservation property [6, 8] can be obtained with the centered flux formulation only, determining the kind of time integration schemes to be used as well [19]. Our implementation includes both flux types.

Having resolved the ambiguity at interfaces, we insert the approximations (6) into the weak formulation (5) and follow the Galerkin procedure

yielding the semi-discrete DG formulation

$$\int_{\mathcal{T}_i} \left(\varphi_i^{q_i} \mu \frac{\partial}{\partial t} \mathbf{H}_h - (\nabla \varphi_i^{q_i}) \times \mathbf{E}_h \right) d^3 \mathbf{r} + \int_{\partial \mathcal{T}_i} \varphi_i^{q_i} (\mathbf{n} \times \mathbf{E}_h^*) d^2 \mathbf{r} = 0, \quad (18a)$$

$$\int_{\mathcal{T}_i} \left(\varphi_i^{q_i} \epsilon \frac{\partial}{\partial t} \mathbf{E}_h + (\nabla \varphi_i^{q_i}) \times \mathbf{H}_h \right) d^3 \mathbf{r} - \int_{\partial \mathcal{T}_i} \varphi_i^{q_i} (\mathbf{n} \times \mathbf{H}_h^*) d^2 \mathbf{r} = 0, \quad (18b)$$

$\forall i = 1..N, \forall q_i = 0..P_i$. The volume integrals are referred to as the mass and stiffness terms, the surface integrals represent face fluxes. Note that no assumptions on the grid regularity have been made in the derivation.

2.3. Employing non-regular grids containing high level hanging nodes

Due to the strictly element-local support of the basis and test functions, the DGM is highly suited for the application on non-regular grids. The actual difference of the refinement levels L_i and L_k of neighboring elements, i.e., the level of hanging nodes, plays a minor role as shown in the following.

Inspecting equations (18) it is seen that the mass and stiffness terms are not affected by the grid regularity as they are strictly local to the element \mathcal{T}_i . The flux term, however, involves neighboring elements as well. Decomposing the surface integral into the six contributing face integrals

$$\int_{\partial \mathcal{T}_i} \varphi_i^{q_i} (\mathbf{n} \times \mathbf{U}_h^*) d^2 \mathbf{r} = \sum_{j=1}^6 \int_{\mathcal{F}_{i,j}} \varphi_i^{q_i} (\mathbf{n}_j \times \mathbf{U}_h^*) d^2 \mathbf{r}, \quad (19)$$

and considering centered fluxes for brevity each of these can be expressed as

$$\int_{\mathcal{F}_{i,j}} \varphi_i^{q_i} (\mathbf{n}_j \times \mathbf{U}_i) d^2 \mathbf{r} + \sum_k \int_{\mathcal{I}_{i,k|j}} \varphi_i^{q_i} (\mathbf{n}_j \times \mathbf{U}_k) d^2 \mathbf{r}. \quad (20)$$

Accounting for the kind of non-regular grids described above, i.e. grids obtained from a regular root tessellation, requires no more than summing up the contributions of all neighboring elements to the total flux. This is independent of the hanging node levels as well as the actual number of neighboring elements. Inserting the approximation (7) into (20) yields

$$\frac{1}{2} \left[\sum_{p_i} \mathbf{n}_j \times \mathbf{u}_i^{p_i} \int_{\mathcal{F}_{i,j}} \varphi_i^{q_i} \varphi_i^{p_i} d^2 \mathbf{r} + \sum_k \sum_{p_k} \mathbf{n}_j \times \mathbf{u}_k^{p_k} \int_{\mathcal{I}_{i,k|j}} \varphi_i^{q_i} \varphi_k^{p_k} d^2 \mathbf{r} \right]. \quad (21)$$

Again, the first integral term does not depend on the grid regularity. Assuming \mathbf{n}_j to be aligned with the z -coordinate and to point towards positive direction it amounts to

$$\int_{\mathcal{F}_{i,j}} \varphi_i^{q_i} \varphi_i^{p_i} d^2 \mathbf{r} = \hat{\varphi}_z^{q_z}(1) \hat{\varphi}_z^{p_z}(1) |\mathcal{F}_z| \quad (22)$$

due to the basis function scaling (13). The second integral term can be expressed as

$$\int_{\mathcal{I}_{i,k|j}} \varphi_i^{q_i} \varphi_k^{p_k} d^2 \mathbf{r} = \hat{\varphi}_z^{q_z}(1) \hat{\varphi}_z^{p_z}(-1) \int_{x_k \cap x_i} \varphi_{x,i}^{q_x} \varphi_{x,k}^{p_x} dx \int_{y_k \cap y_i} \varphi_{y,i}^{q_y} \varphi_{y,k}^{p_y} dy. \quad (23)$$

In this case the orthogonality property of the basis functions is lost due to non-identical supports of φ_i and φ_k . We gather the terms (22) and (23) in the interior and exterior flux matrices \mathbf{F}^- and \mathbf{F}^+ . Following to the usual notation the sign indicates the evaluation from the interior and exterior side of the interface. Any non-regularity of the grid is now concealed within \mathbf{F}^+ , which reduces to the standard form on regular grids.

For high level hanging nodes the number of integrals to compute quickly becomes large, imposing a heavy computational burden if integration is performed at run time. However, as the integrals $\int_{d_k \cap d_i} \varphi_{d,i}^{q_d} \varphi_{d,k}^{p_d} dr_d$ in (23) do not include the actual approximation but basis functions only, they can be precomputed analytically (making use of the master basis functions) and stored in tabulated form in the code. This has to be done for all combinations of p_d and q_d as well as for each possible edge overlap according to the respective difference in the refinement levels ΔL_d (cf. Fig. 1). The number of possible overlaps grows as $2^{\Delta L_d}$. We tabulated the integrals up to $\Delta L_d = 6$ and for basis functions up to order six, yielding 247 matrices $\mathbf{I}_{\Delta L}$ of size 7×7 . In the isotropic refinement case $\Delta L_d = 6$ corresponds to one element interfacing with $(2^6)^2 = 4096$ neighbors. In the case of even larger differences in the refinement levels of neighboring elements, which are unlikely to occur a numerical integration is invoked at run time. If the neighboring element has a smaller instead of higher refinement level the respective transposed matrix $(\mathbf{I}_{\Delta L})^T$ is applied. For upwind fluxes, the interior and exterior flux matrices do not change, however, they are applied to both, the electric and the magnetic field due to (16).

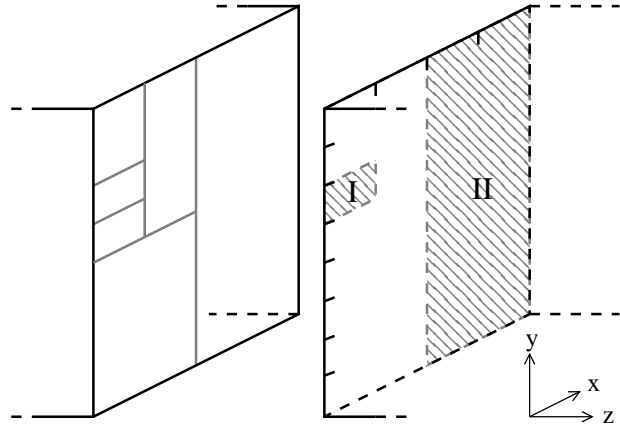


Figure 1: Example of a non-matching interface. Black lines indicate edges of the root tesselation, gray lines indicate edges of refined elements. In the figure the interfaces are separated along the z -axis for a better visualization. The left hand root element has been refined several times, the right hand element is at root level. The interface I connects an element of refinement levels $(2, 3, L_z)$ with the root level element. The tick marks indicate possible locations for the imprint of elements of these refinement levels. The actual imprint on the root element face fills the first and sixth slab along the x - and y -axis, respectively. The interface II fills the respective second slab along the x -axis.

In order to further enhance computational performance, all combinations of $\hat{\varphi}^{qd}(\pm 1)\hat{\varphi}^{pd}(\pm 1)$ and the integrals $\int_{\hat{\mathcal{T}}_d} \left(\frac{d}{d\hat{r}_d} \hat{\varphi}^{qd} \right) \hat{\varphi}^{pd} d\hat{r}_d$ arising from the stiffness terms of (18) are evaluated and tabulated as well. Precomputing the interface integrals maintains the high computational efficiency of the DG methods also for non-regular grids. Using matrix notation, the semi-discrete DG Maxwell equations (18) read

$$\frac{d}{dt} \begin{pmatrix} \mathbf{M}_\mu \mathbf{h} \\ \mathbf{M}_\epsilon \mathbf{e} \end{pmatrix} = \begin{pmatrix} \gamma(\mathbf{F}^- + \mathbf{F}^+) \mathbf{Z} & -\mathbf{S} + (\mathbf{F}^- + \mathbf{F}^+) \\ \mathbf{S} - (\mathbf{F}^- + \mathbf{F}^+) & \gamma(\mathbf{F}^- + \mathbf{F}^+)/\mathbf{Z} \end{pmatrix} \begin{pmatrix} \mathbf{h} \\ \mathbf{e} \end{pmatrix}, \quad (24)$$

where \mathbf{S} and \mathbf{Z} denotes the stiffness and impedance matrix. The matrix operator on the right hand side of (24) represents a weak DG curl operator. Choosing γ as either zero or one yields centered or upwind fluxes, respectively. By applying centered fluxes the Hamiltonian structure of Maxwell's equations in continuum is preserved, whereas upwind fluxes lead to a mixed form. Symplectic explicit time integration can be applied in the former case but not in the latter one [19]. For examples of symplectic time integration for Maxwell's equations in the DG framework see, e.g., [6, 8, 20]. In [3, 5] upwind fluxes and Runge-Kutta schemes are applied for the time integration, where

the latter one is concerned with Maxwell's equations.

3. Local refinement techniques

The adaptation techniques presented in the following are based on projections between the finite element spaces introduced in (12). The projection operators have been introduced in [16], however, they are included for completeness. Also, we address the issue of stability in depth and amended this section with examples.

The approximation f_h to a given function f in the FES \mathcal{V}^P is obtained by performing an orthogonal projection. The projection is carried out in an element-wise manner, by means of the projection operator Π^P given by

$$f_i = \sum_p \Pi^p(f)_{\mathcal{T}_i} \varphi_i^p = \sum_p \frac{(\varphi_i^p, f)_{\mathcal{T}_i}}{(\varphi_i^p, \varphi_i^p)_{\mathcal{T}_i}} \varphi_i^p, \quad (25)$$

where $(u, v)_{\mathcal{T}_i}$ denotes the inner product $\int_{\mathcal{T}_i} uv \, d\mathbf{r}$ on the element \mathcal{T}_i with the associated 2-norm $(u, u)_{\mathcal{T}_i} = \|u\|_{\mathcal{T}_i}^2$. When applied successively to all elements and all components of given initial conditions of the electric field, $\mathbf{E}(t = t_0)$, and the magnetic field, $\mathbf{H}(t = t_0)$, the respective DG approximations \mathbf{E}_h and \mathbf{H}_h are obtained. These approximations are optimal in the sense that the projection errors $\mathcal{E}_d = U_d - U_{d,h}$ are orthogonal to the space of basis functions \mathcal{V}^P

$$(\mathcal{E}_d, \varphi_i^p)_{\mathcal{T}_i} = 0; \quad \forall p \in [0, P], \varphi_i^p = \hat{\varphi}^p \circ G_i^{-1}, \varphi^p \in \mathcal{V}^P \quad (26)$$

3.1. *h*-Refinement

As stated above *h*-refinement is achieved by means of element bisections along the coordinate directions, where we allow for anisotropic refinements. The refined elements are referred to as the left and right hand side element \mathcal{T}_l and \mathcal{T}_r with basis functions denoted as $\hat{\varphi}_l^l$ and $\hat{\varphi}_r^r$ spanning the spaces \mathcal{V}_l^L and \mathcal{V}_r^R in a full analogy to \mathcal{V}^P defined in (12). The approximation orders L_d and R_d in each child element do not have to be identical, neither are they required to be equal to the respective order P_d of the parent element. The direct sum of the spaces \mathcal{V}_l and \mathcal{V}_r is denoted by \mathcal{V}^+

$$\mathcal{V}^+ = \mathcal{V}_l \oplus \mathcal{V}_r. \quad (27)$$

In the following, the projection (25) can be applied in order to project an approximation given in an element \mathcal{T}_i to the FES associated with an h -refined or h -reduced element. For h -refinement this yields

$$(\mathbf{u}_i)_l^l = \Pi_l^l(\mathbf{U}_i)_{\mathcal{T}_i}, \quad (\mathbf{u}_i)_r^r = \Pi_r^r(\mathbf{U}_i)_{\mathcal{T}_i}. \quad (28)$$

Due to the tensor product character of the basis, this can be expressed as

$$(\mathbf{u}_i)_l^l = \sum_p \mathbf{u}_i^p \Pi_l^l(\varphi_i^p)_{\mathcal{T}_i} = \sum_p \mathbf{u}_i^p \Pi_l^{l_x}(\varphi_i^{p_x})_{\mathcal{T}_{x,1}} \Pi_l^{l_y}(\varphi_i^{p_y})_{\mathcal{T}_{y,1}} \Pi_l^{l_z}(\varphi_i^{p_z})_{\mathcal{T}_{z,1}} \quad (29)$$

for the left and right child, respectively. If refinement is carried out along one coordinate only, e.g. x , this further simplifies to

$$(\mathbf{u}_i)_l^l = \delta_{l_y p_y} \delta_{l_z p_z} \sum_{p_x} \mathbf{u}_i^p \Pi_l^{l_x}(\varphi_i^{p_x})_{\mathcal{T}_{x,1}} = \delta_{l_y p_y} \delta_{l_z p_z} \sum_{p_x} \mathbf{u}_i^p \frac{(\varphi_l^{l_x}, \varphi_i^{p_x})_{\mathcal{T}_{x,1}}}{|\mathcal{T}_{x,1}|}, \quad (30)$$

where δ denotes the Kronecker delta. Note that above we loop over p_x , whereas in (29) the loop parameter is p . As, moreover, $(\varphi_l^{l_x}, \varphi_i^{p_x})_{\mathcal{T}_{x,1}}$ vanishes for any $p_x < l_x$, we can limit the above loop to the range $[l_x, P_{x,i}]$, which reduces the number of addends to the minimum possible.

For the merging of elements, the approximation within the parent element, \mathcal{T}_i , is considered to be given piece-wise within its child elements. The projection reads

$$\mathbf{u}_i^p = \Pi^p((\mathbf{U}_i)_l + (\mathbf{U}_i)_r)_{\mathcal{T}_i} = \Pi^p((\mathbf{U}_i)_l)_{\mathcal{T}_i} + \Pi^p((\mathbf{U}_i)_r)_{\mathcal{T}_i}, \quad (31)$$

where the simplifications (29) and (30) apply.

3.2. p -Refinement

For the case of p -enrichments, the local FES are amended with the (P_d+1) order basis functions

$$\mathcal{V}_i^{P+1} = \mathcal{V}_i^P \cup \{\varphi_{d,i}^{P_d+1}\}, \quad (32)$$

where any (non-zero) number of the local maximum approximation orders P_d may be increased. Also, an enrichment by more than one higher order basis function is possible. Formally, we perform the orthogonal projection (25), however, due to the orthogonality property of the basis functions the coefficients $\mathbf{u}_i^{0..P}$ remain unaltered under a projection from \mathcal{V}_i^P to \mathcal{V}_i^{P+1} . Practically, we simply extend the local vectors of coefficients \mathbf{u}_i with the new coefficients \mathbf{u}_i^{P+1} , which are initialized to zero.

Conversely, for the case of a p -reduction, the local FES is reduced by discarding the P_d -order basis functions

$$\mathcal{V}_i^{P-1} = \mathcal{V}_i^P \setminus \{\varphi_{d,i}^{P_d}\}. \quad (33)$$

Again, by following the orthogonality argument, we find that the coefficients \mathbf{u}_i^P are deleted from the local vectors of coefficients while the coefficients $\mathbf{u}_i^{0..P-1}$ remain unaltered.

We denote by $\Pi_{\mathcal{T}}$ the projection of the global approximation $(\mathbf{E}_h, \mathbf{H}_h)$ from the current discretization to another one obtained by local h - and p -adaptations.

3.3. Optimality, Efficiency and Stability

3.3.1. Optimality

An approximation \mathbf{U}_h with coefficients according to (25) is optimal in the sense of (26). The approximations within refined and merged elements with coefficients obtained through the orthogonal projections (28) and (31) are, hence, optimal in the same sense.

If $L_d \geq P_d$ and $R_d \geq P_d$ holds true for all d , the FES \mathcal{V} is a subspace of \mathcal{V}^+ (cf. (27)) and every function of \mathcal{V} is representable in \mathcal{V}^+ but not vice versa. In this case, a given approximation is exactly represented within an element under h -refinement but not under h -reduction. See Fig. 2 for an example.

3.3.2. Efficiency

Since the projections (28) for performing h -refinement are independent of the actual approximation, we also tabulated the projection operators $\Pi_l^{l_d}$ and $\Pi_r^{r_d}$ (expressed in master basis functions) yielding the matrix operators $(\boldsymbol{\Pi}_l)^+$ and $(\boldsymbol{\Pi}_r)^+$, where the superscript denotes that the refinement level L is increased. Accordingly, we make use of the matrix operators $(\boldsymbol{\Pi}_l)^-$ and $(\boldsymbol{\Pi}_r)^-$ for evaluating the projections of (31) in the case of element merging. The matrix operators are related as

$$(\boldsymbol{\Pi}_l)^- = 2(\boldsymbol{\Pi}_l^+)^T, \quad (\boldsymbol{\Pi}_r)^- = 2(\boldsymbol{\Pi}_r^+)^T. \quad (34)$$

This allows for the computation of the approximations within adapted elements by means of efficient matrix-vector multiplications. As all projection matrices are triangular the evaluation can be carried out as an in-place operation requiring no allocation of temporary memory.

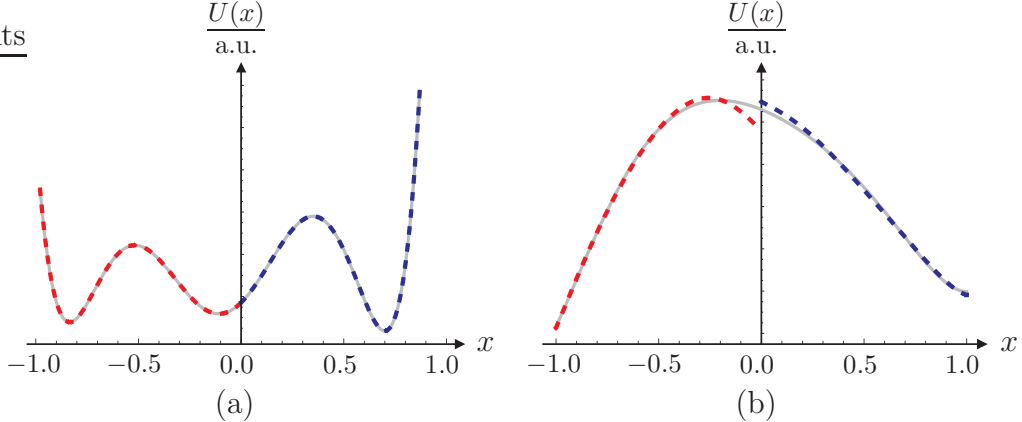


Figure 2: Projection based grid refinement and coarsening in one dimension. In (a) the projection of a given approximation (gray) to the left and right hand side child elements and the respective obtained approximations are shown (dashed, red/blue). If $L_x \geq P_x$ and $R_x \geq P_x$, the approximations of the parent and child elements agree point-wise. The projection to a merged element shown in (b) can, in general, not be exact due to the discontinuity.

3.3.3. Stability

The global approximation associated with an adapted grid is computed as $(\Pi_{\mathcal{T}} \mathbf{E}_h, \Pi_{\mathcal{T}} \mathbf{H}_h)$. It can be considered as initial conditions applied on the new discretization obtained by performing the refinement operations. Assuming stability of the time stepping scheme (cf. [5, 6, 8]), it is sufficient to show that the application of the projection operators at some time t^* does not increase the electromagnetic energy associated with the approximate DG solution, i.e.,

$$W_h(\mathbf{E}_h(t^*), \mathbf{H}_h(t^*)) \geq W_h(\Pi_{\mathcal{T}} \mathbf{E}_h(t^*), \Pi_{\mathcal{T}} \mathbf{H}_h(t^*)). \quad (35)$$

In this case it follows $W_h(t_0)) \geq W_h(t^*) \geq W_h(T)$ and, thus, stability of the adaptive scheme.

Following (3) the energy associated with element \mathcal{T}_i is given as

$$W_i = \int_{\mathcal{T}_i} \frac{1}{2} (\epsilon \mathbf{E}_i^2 + \mu \mathbf{H}_i^2) d^3 \mathbf{r} = \frac{1}{2} |\mathcal{T}_i| (\epsilon_i \|\mathbf{e}_i\|_2^2 + \mu_i \|\mathbf{h}_i\|_2^2). \quad (36)$$

As a consequence of (29), it is sufficient to show that the energy (36) is non-increasing during any adaptation involving one coordinate only.

h-Refinement. For the following discussion of stability it is assumed that refinement is carried out along the x -coordinate. Also we assume the maximum

approximation orders L, R and P to be identical. It is clarified later, that this does not pose a restriction to the general validity of the results.

In the case of h -refinement, the operators Π_l^+ and Π_r^+ project from the space \mathcal{V} to the larger space \mathcal{V}^+ . Following the argument of paragraph 3.3.1 on optimality, any function defined in the space \mathcal{V} is exactly represented in \mathcal{V}^+ . The conservation of the discrete energy is a direct consequence² as the approximation in the parent and child elements are point-wise identical.

We find the following relation for the 2-norms of the respective local vectors of coefficients

$$\begin{aligned} W_i &= (W_i)_l + (W_i)_r \\ \frac{\Delta x}{2} (\epsilon_i \|\mathbf{e}_i\|_2^2 + \mu_i \|\mathbf{h}_i\|_2^2) &= \frac{\Delta x}{4} (\epsilon_i \|\mathbf{(e}_i)_l\|_2^2 + \mu_i \|\mathbf{(h}_i)_l\|_2^2 + \epsilon_i \|\mathbf{(e}_i)_r\|_2^2 + \mu_i \|\mathbf{(h}_i)_r\|_2^2) \\ 2(\epsilon_i \|\mathbf{e}_i\|_2^2 + \mu_i \|\mathbf{h}_i\|_2^2) &= \epsilon_i (\|\mathbf{(e}_i)_l\|_2^2 + \|\mathbf{(e}_i)_r\|_2^2) + \mu_i (\|\mathbf{(h}_i)_l\|_2^2 + \|\mathbf{(h}_i)_r\|_2^2). \end{aligned} \quad (37)$$

The exemplary parent element approximation plotted in Fig. 2a has a maximum order of $P = 6$ with all coefficients equal to one. The coefficients of the child element approximations and the square values of their 2-norms are given in Tab. 1. If the vector \mathbf{u} is considered to be either the vector of coefficients of the electric field \mathbf{e} or the magnetic field \mathbf{h} the result agrees with (37).

	u_0	u_1	u_2	u_3	u_4	u_5	u_6	$\ \mathbf{u}\ _2^2$
$U(x)$	1.0000	1.0000	1.0000	1.0000	1.0000	1.0000	1.0000	7.0000
$U(x)_l$	0.2574	-0.1355	-0.2606	-0.1446	0.4276	-0.1563	0.0156	0.3808
$U(x)_r$	1.7426	1.5631	1.6819	2.0399	1.0494	0.2181	0.0156	13.6192

Table 1: Parent and child element coefficients of the function plotted in Fig. 2a

The h -coarsening operators Π_l^- and Π_r^- project a function from the space \mathcal{V}^+ to the smaller space \mathcal{V} . Since \mathcal{V} is a subspace of \mathcal{V}^+ , it is immediately concluded that, in general, energy is lost during the coarsening process. The discrete energy can only be preserved if the union of the left and right hand functions is an element of the smaller space \mathcal{V} . Starting with the coefficients of the child elements, given in Tab. 1, the parent element coefficients are exactly recovered and the discrete energy is preserved.

In particular, it can be shown from algebraic properties of the projection matrices, that the discrete energy for arbitrary fine grid coefficients is always

²Identical material properties are assumed for the parent and child elements.

non-increasing during h -coarsening. First, the $(P_d \times 2P_d)$ projection matrix Π^- is defined as

$$\Pi^- = \begin{pmatrix} \Pi_l^- & \Pi_r^- \end{pmatrix}. \quad (38)$$

The coefficients of the child elements are gathered in one vector $(\mathbf{u}_i)^+$

$$(\mathbf{u}_i)^+ = \begin{pmatrix} (\mathbf{u}_i)_l \\ (\mathbf{u}_i)_r \end{pmatrix}. \quad (39)$$

Then, the coefficients of the parent element are given as

$$\mathbf{u}_i = \Pi^- (\mathbf{u}_i)^+, \quad (40)$$

which is equivalent to Eqn. (31). Using (36) and (37), the following must hold true in order to guarantee a non-increasing discrete energy

$$\begin{aligned} 2\|\mathbf{u}_i\|_2^2 &\stackrel{!}{\leq} \|(\mathbf{u}_i)^+\|_2^2 \\ 2\mathbf{u}_i^T \mathbf{u}_i &\stackrel{!}{\leq} ((\mathbf{u}_i)^+)^T (\mathbf{u}_i)^+ \\ 2(\Pi^- (\mathbf{u}_i)^+)^T \Pi^- (\mathbf{u}_i)^+ &\stackrel{!}{\leq} ((\mathbf{u}_i)^+)^T (\mathbf{u}_i)^+ \\ \frac{((\mathbf{u}_i)^+)^T (\Pi^-)^T \Pi^- (\mathbf{u}_i)^+}{((\mathbf{u}_i)^+)^T (\mathbf{u}_i)^+} &\stackrel{!}{\leq} \frac{1}{2}. \end{aligned} \quad (41)$$

In order to fulfill this it is sufficient to demand

$$\max \left\{ \text{eig} \left((\Pi^-)^T \Pi^- \right) \right\} \leq \frac{1}{2}. \quad (42)$$

Since the matrix $((\Pi^-)^T \Pi^-)$ has the P_d -times degenerated eigenvalues $1/2$ and 0 this is always fulfilled.

The coefficients for the example shown in Fig. 2b are listed in Table 2. The sum of the 2-norms for the left and right hand child vectors of coefficients yields 1.9003 while twice the value obtained for the parent element evaluates to 1.8996. Thus, energy was lost during h -coarsening.

p-Refinement. In order to show stability of the p -adaptation we again consider the energy stored in an element given by (36). In the case of p -enrichment, the local vectors of DoF are extended by the coefficients corresponding to the $(P+1)$ -order basis functions. Since these coefficients are initialized to zero, it holds true

$$\|(\mathbf{u})^P\|_2^2 = \|(\mathbf{u})^P\|_2^2 + 0 = \|(\mathbf{u}_{0..P})^{P+1}\|_2^2 + \|(\mathbf{u}_{P+1})^{P+1}\|_2^2 = \|(\mathbf{u})^{P+1}\|_2^2. \quad (43)$$

	u_0	u_1	u_2	u_3	$\ \mathbf{u}\ _2^2$
$U(x)$	0.9500	-0.0433	-0.2073	0.0498	0.9498
$U(x)_1$	1.0000	0.2000	-0.1000	-0.0100	1.0501
$U(x)_r$	0.9000	-0.2000	-0.0100	0.0100	0.8502

Table 2: Parent and child element coefficients of the function plotted in Fig. 2b

The discrete energy is exactly conserved.

In the case of a p -reduction, the coefficients assigned to the highest order basis functions are removed from the vectors of DoF. Consequently, it holds true

$$\|(\mathbf{u})^P\|_2^2 = \|(\mathbf{u}_{0..P-1})^P\|_2^2 + \|(\mathbf{u}_P)^P\|_2^2 \leq \|(\mathbf{u}_{0..P-1})^P\|_2^2 = \|(\mathbf{u})^{P-1}\|_2^2, \quad (44)$$

and the discrete energy is either preserved or otherwise reduced. If the decision for reducing the order is a correct one, the highest order coefficients are small and the induced energy loss is small.

In the discussion of stability for h -adaptations it was assumed that the maximum approximation orders L , R and P are identical. After showing that p -adaptation does not increase the electromagnetic energy either, it can be concluded that this assumption does not restrict the validity of the results obtained as the problem can be reduced to performing h - and p -adaptations sequentially.

Finally, we will make some remarks on mixed h - and p -adaptations. If an h -coarsening goes along with a p -enrichment, the latter should be performed first. It amounts to a projection to the superspace \mathcal{V}_h^{P+1} . Projection errors are limited to the projection onto the space \mathcal{V}_{2h}^{P+1} . If the projections are carried out in reversed order the final space is \mathcal{V}_{2h}^{P+1} as well, however, the second projection from \mathcal{V}_{2h}^P adds zeros to the local vector of DoF only, resulting in an increased overall projection error. On the contrary, if an h -refinement goes along with a p -reduction, the former should be carried out first for the same reason. However, the two adaptations can be performed simultaneously by employing projection matrices of the size $(P_d^{\text{new}} \times P_d^{\text{old}})$.

4. Application example

We consider the backscattering of a wide-band electromagnetic pulse from a passive radar reflector. The reflector is illuminated off-center by a horn antenna, which emits a Gaussian-modulated sinusoidal pulse covering the

frequency range from 20 to 30 GHz. The initial waveform is a TE_{10} (transverse electric) wave. The setup is depicted in Fig. 3, where the antenna is shown in a cut view along with contour plots of the pulse at two instances in time ($t = 1$ ns and $t = 10$ ns). Table 3 lists the parameters and dimensions. We use this example as a test case for checking the ability of our implementation [21] to handle large problems and simulate the full scattering process starting from the excitation inside the waveguide to the recording of the reflected fields at the same position. The total propagation distance is about sixty wavelengths.

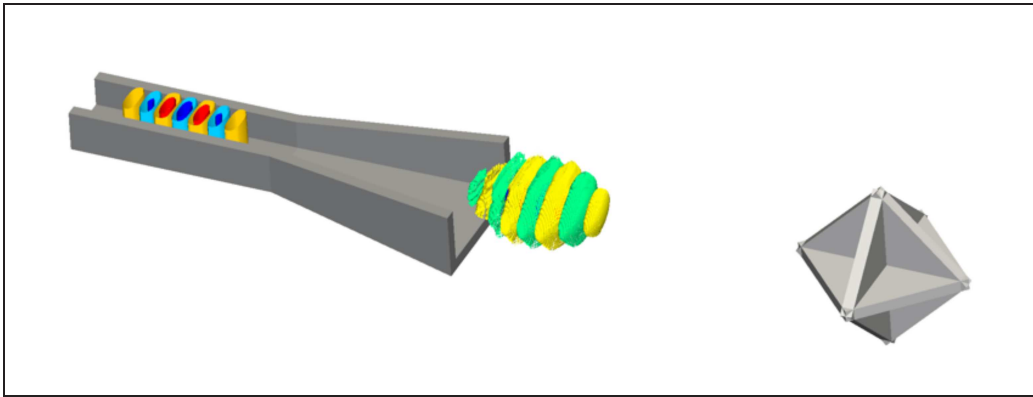


Figure 3: Scattering setup consisting of a horn antenna (in cut view) illuminating a radar reflector. The antenna emits a broadband electromagnetic waveform, whose electric field contours are depicted at two instances in time.

Parameter	Value
Waveform mode	TE_{10}
Waveform frequency range	20 – 30 GHz
Waveguide type	WR-62
Waveguide width	15.8 mm
Waveguide height	7.9 mm
Horn width	39.7 mm
Horn height	29.0 mm
Horn depth	67.5 mm

Table 3: Setup parameters and dimensions

The initial discretization consists of $45 \times 35 \times 100 = 157,500$ elements, which are subject to dynamic mesh refinement. During the simulation the

number of elements varies due to the dynamically adapted mesh. After scattering from the reflector took place the number grew strongly and reached close to 800,000 elements. The maximum h -refinement level is two and the element order varies from zero to four resulting in slightly more than 55 million DoF and 120,000 time steps for the full-wave simulation. For comparison, we note that employing the finest mesh resolution globally as well as fourth order approximations uniformly would lead to approximately 7.5 billion DoF.

We emphasize that the simulations were carried out on a single machine. The implementation takes full advantage of multi-core capabilities through OpenMP parallelization. The numerous run-time memory allocations and deallocations are handled through a specialized memory management library based on memory blocking, which we implemented for supporting the main code [22].

In [16] we presented an hp -adaptation strategy, which combines an error estimator based on the element residual [23] and a shock detector [24]. The former one is employed for marking elements for refinement/derefinement, whereas the latter one is applied for finding the hp -decision, i.e., the type of adaptation to be carried out. This strategy was shown to yield good results at comparatively low computational costs. However, its extension to non-regular grids in three-dimensional space is not yet completed. Therefore, we resorted to employing an adaptation indicator based on physical properties of the approximate solution. One possible indicator is the local energy density, introduced in (3), which we chose for controlling the adaptation procedure. Fig. 4 depicts cut-views of the y -component of the electric field and the respective discretization at three instances in time. Note that the scaling of the electric field differs for every time instance, which is necessary to allow for a visual inspection.

The enlargement shows details of the computational grid. All elements are of hexahedral kind, however, we make use of the common tensor product visualization technique (cf. [25, 26]) using embedded tetrahedra for displaying the three tensor product orders (out of which only P_x and P_z are visible in the depicted $x-z$ -plane). As we employed isotropic h - as well as p -refinement all tetrahedra associated with one element share the same color. Fig. 5 shows plots of the outgoing and reflected waveform recorded along the waveguide center.

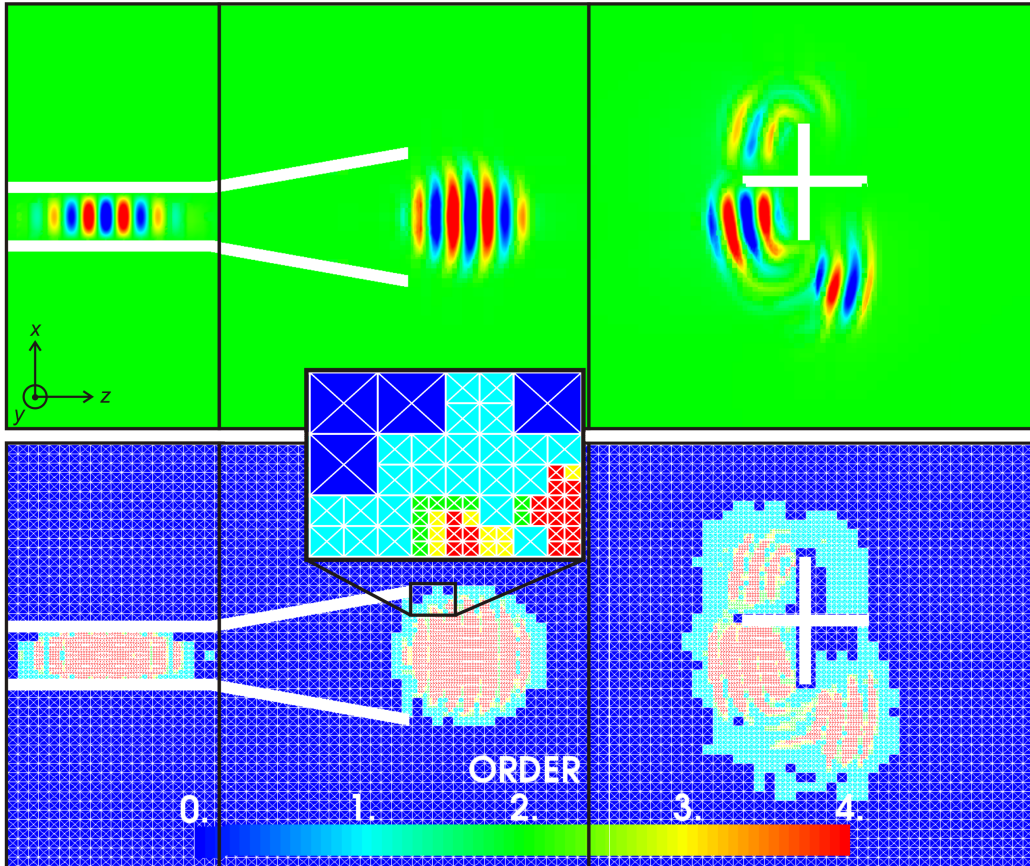


Figure 4: Visualizations of the y -component of the electric field (top panel) and the computational grid (bottom panel) at three instances in time. The enlargement shows details of the grid. We employ hexahedral elements for the computation but make use of embedded tetrahedra for displaying the tensor product orders in the grid view. As isotropic p -refinement was employed in this examples all tetrahedra associated with one element share a common color. Note that different scalings are used for the time instances in the top panel.

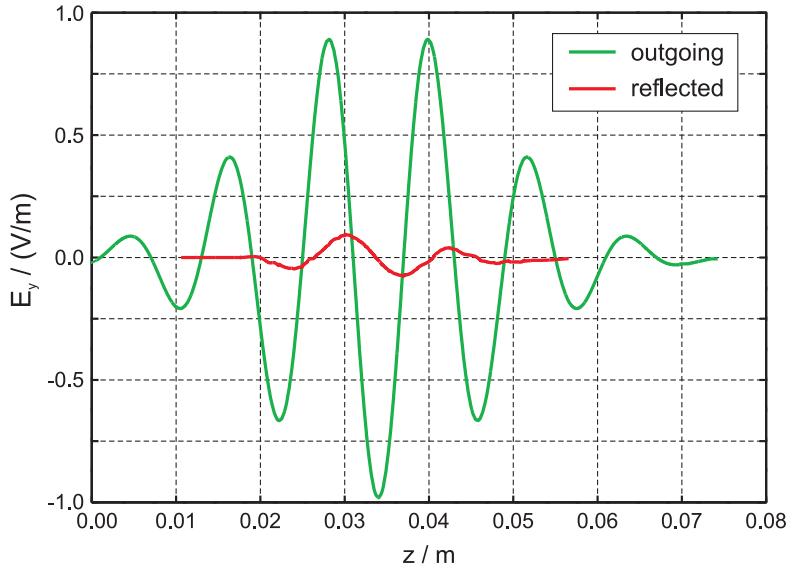


Figure 5: Plots of the outgoing and reflected waveform along the waveguide center.

5. Conclusions

We presented a discontinuous Galerkin formulation for non-regular hexahedral meshes and showed that hanging nodes of high level can easily be included into the framework. In fact, any non-regularity of the grid can be included in a single term reflecting the contribution of neighboring elements to the local interface flux. We demonstrated that the method can be implemented such that it maintains its computational efficiency also on non-regular and locally refined meshes as long as the mesh is derived from a regular root tessellation by means of element bisections. This is achieved by extensive tabulations of flux and projection matrices, which are obtained through (analytical) precomputations of integral terms.

We also presented local refinement techniques for h - and p -refinements, which are based on projections between finite element spaces. These projections were shown to guarantee minimal projection errors in the L^2 sense and to lead to an overall stable time-domain scheme.

As an application example the backscattering of a broadband waveform from a radar reflector was considered, where the total wave propagation distance corresponds to approximately sixty wavelengths. We chose to drive the grid adaptation using the energy density as refinement indicator. This procedure is an intermediate step towards error driven hp -adaptation, which we

presented for one-dimensional setups in [16]. Other future work includes the incorporation of boundary conforming block-structured hexahedral meshes, which is subject of a forthcoming article.

References

- [1] W. Reed, T. Hill, Triangular mesh methods for the neutron transport equation, Tech. rep., Los Alamos Scientific Laboratory Report (1973).
- [2] P. LeSaint, P.-A. Raviart, On a finite element method for solving the neutron transport equation, Academic Press, 1974, pp. 89–123.
- [3] B. Cockburn, C. Shu, Runge–kutta discontinuous galerkin methods for convection-dominated problems, *J Sci Comput* 16 (3) (2001) 173–261.
- [4] J. S. Hesthaven, T. Warburton, *Nodal Discontinuous Galerkin Methods*, Springer, 2008.
- [5] J. S. Hesthaven, T. Warburton, Nodal high-order methods on unstructured grids i. time-domain solution of maxwell’s equations, *J Comput Phys* 181 (1) (2002) 186–221.
- [6] L. Fezoui, S. Lanteri, S. Lohrengel, S. Piperno, Convergence and stability of a discontinuous galerkin time-domain method for the 3d heterogeneous maxwell equations on unstructured meshes, *ESAIM-Math Model Num* 39 (6) (2005) 1149–1176.
- [7] G. Cohen, X. Ferrieres, S. Pernet, A spatial high-order hexahedral discontinuous Galerkin method to solve Maxwell’s equations in time domain, *J Comput Phys* 217 (2) (2006) 340–363.
- [8] E. Gjonaj, T. Lau, S. Schnupp, F. Wolfheimer, T. Weiland, Accurate modelling of charged particle beams in linear accelerators, *New J Phys* 8 (2006) 1–21.
- [9] D. Wirasaet, S. Tanaka, E. J. Kubatko, J. J. Westerink, C. Dawson, A performance comparison of nodal discontinuous galerkin methods on triangles and quadrilaterals, *Int J Numer Meth Fluids* 64 (10-12) (2010) 1336–1362.

- [10] K. Bey, J. Oden, hp-version discontinuous galerkin methods for hyperbolic conservation laws, *Comput Method Appl M* 133 (1996) 259–286.
- [11] C. Baumann, J. Oden, A discontinuous hp finite element method for convection–diffusion problems, *Comput Method Appl M* 175 (3-4) (1999) 311–341.
- [12] P. Houston, E. Sli, hp-adaptive discontinuous galerkin finite element methods for first-order hyperbolic problems, *SIAM J Sci Comput* 23 (2001) 1226–1252.
- [13] I. Perugia, D. Schötzau, P. Monk, Stabilized interior penalty methods for the time-harmonic maxwell equations, *Comput Method Appl M* 191 (41) (2002) 4675–4698.
- [14] I. Perugia, D. Schotzau, The hp-local discontinuous galerkin method for low-frequency time-harmonic maxwell equations, *Math Comput* 72 (243) (2003) 1179–1214.
- [15] P. Houston, I. Perugia, D. Schotzau, Energy norm a posteriori error estimation for mixed discontinuous galerkin approximations of the maxwell operator, *Comput Method Appl M* 194 (2-5) (2005) 499–510.
- [16] S. Schnepp, T. Weiland, Discontinuous galerkin methods with transient hp-adaptation, *Radio Sci* 46 (2011) RS0E03.
- [17] R. J. LeVeque, *Numerical Methods for Conservation Laws*, Birkhäuser, 1990.
- [18] S. Schnepf, Space-time adaptive methods for beam dynamics simulations, Ph.D. thesis, TU Darmstadt (2009).
- [19] S. Schnepf, E. Gjonaj, T. Weiland, A hybrid finite integration–finite volume scheme, *J Comput Phys* 229 (11) (2010) 4075–4096.
- [20] N. Canouet, L. Fezoui, S. Piperno, Discontinuous galerkin time-domain solution of maxwell’s equations on locally-refined nonconforming cartesian grids, *COMPEL* 24 (4) (2005) 1381–1401.

- [21] SMOVE, A program for the adaptive simulation of electromagnetic fields and arbitrarily shaped charged particle bunches using moving meshes, technical documentation: <http://www.graduate-school-ce.de/files2/schnepp/SMOVE/>.
- [22] DynaMO, A dynamic memory organization library, technical documentation: <http://www.graduate-school-ce.de/files2/schnepp/DynaMO/>.
- [23] B. Cockburn, Discontinuous galerkin methods, ZAMM-Z Angew Math Me 83 (11) (2003) 731–754.
- [24] L. Krivodonova, J. Xin, J. Remacle, N. Chevaugeon, J. Flaherty, Shock detection and limiting with discontinuous Galerkin methods for hyperbolic conservation laws, Appl Numer Math 48 (3-4) (2004) 323–338.
- [25] P. Solin, J. Cerveny, I. Dolezel, Arbitrary-level hanging nodes and automatic adaptivity in the hp-fem, Math Comput Simulat 77 (1) (2008) 117 – 132.
- [26] L. Demkowicz, Computing with HP-Adaptive Finite Elements: Volume 1: One and Two Dimensional Elliptic and Maxwell Problems, Chapman & Hall/CRC, 2007.